Producing Known Complex Modulation Signals for Characterization of Coherent Optical Receivers

Tasshi Dennis, *Member, OSA* and Bernd Nebendahl

***Abstract*—We introduce a family of complex modulation signals that are generated as patterns over the real and imaginary plane for characterization of coherent optical receivers. The properties of the complex signals can be predicted from first principles, enabling quantitative comparisons between measurement and theory. An optical heterodyne technique with phase-locked loops for frequency control and narrow-band lasers was used to create the known signals, providing temporal stability and ease of operation. The modulation patterns could be made arbitrarily intricate simply by selection of the heterodyne frequencies, with no hardware modifications. The technique is capable of generating signals with frequencies of more than 100 GHz. A real-time optical modulation analyzer was used to visualize the modulation patterns and illustrate their properties. In turn, we used the modulation patterns to characterize the coherent receiver within the modulation analyzer, thereby examining its demodulation algorithm, software processing, digital filtering, and detector gain balance. By working with known modulation patterns, we were able to create an error vector waveform to allow quantitative evaluation of measured signals as they spanned the complex plane.**

***Index Terms*—Coherent communications, complex modulation formats, heterodyne, metrology, phase lock loop.**

I. Introduction

COHERENT optical communications techniques utilizing complex modulation formats have become the preferred method for achieving data rates of 100 Gb/s and beyond on a single optical carrier. Complex formats modulate both the amplitude and phase to increase the spectral efficiency of a network by increasing the number of bits per transmitted symbol [1], [2]. In general, to fully demodulate an optical signal with a complex format requires a coherent optical receiver [1], whether to recover the transmitted bits of information or to visualize the signal for monitoring purposes. The coherent receiver removes the carrier frequency by optically mixing the signal with a local oscillator, while at the same time preserving the amplitude and phase modulation information. As such, the coherent receiver is a crucial network component, but requires proper characterization to achieve highly accurate, quantitative performance. One method to obtain this characterization is to quantify how well a receiver can measure complex signals that are known from first principles or have been accurately characterized.

Manuscript received March 14, 2013; revised May 21, 2013 and August 28, 2013; accepted September 16, 2013. Date of publication October 1, 2013; date of current version November 8, 2013.

T. Dennis is with the Department of Quantum Electronics and Photonics, National Institute of Standards and Technology, Boulder, CO 80305 USA (e-mail: tasshi@boulder.nist.gov).

B. Nebendahl is with Agilent Technologies, 71034 Böblingen, Germany (e-mail: Bernd_Nebendahl@Agilent.com).

Color versions of one or more of the figures in this paper are available online at http://ieeexplore.ieee.org.

Digital Object Identifier 10.1109/JLT.2013.2284157

A variety of measurement methods exist that are capable of characterizing both the magnitude and phase of complex modulated optical signals, including, but not limited to quadrature detection with electrical sampling [3], linear optical sampling [5], [6], nonlinear optical sampling [7], and coherent spectrum analysis [3]. However, as varied as these measurement methods may be, all ultimately incorporate or function as a coherent receiver, requiring some form of calibration.

In addition to the well-known challenge of calibrating the amplitude and time axes of a direct-detection receiver or an oscilloscope with an optical front end [8], [9], a coherent optical receiver must also have a calibrated phase axis. Viewed differently, the in-phase and quadrature amplitude axes of a coherent receiver must be simultaneously well characterized at all points in the complex plane. Ideally, the measurement of a signal that is uniformly distributed, for example 64-QAM, will be measured accurately and displayed free of distortions in both the in-phase and quadrature directions.

Calibration of the complex measurement plane is difficult because the generation of modulated test signals is inherently complicated, and the devices used typically have an imperfect response. For example, the dual-parallel Mach–Zehnder modulator can generate an arbitrary complex signal; however, its amplitude response is not perfectly linear, and the device must be operated at three bias points that drift. Such imperfections alone are not a problem if they can be independently verified, but therein resides the problem that the available metrology tools may lack the necessary calibration. Furthermore, many metrology tools based on coherent receivers may rely heavily on software algorithms in order to present a signal in a meaningful way, by correcting for carrier phase drift, polarization multiplexing, and gain variations [10], [11]. This makes them considerably tolerant to their own instrument imperfections, but may also unknowingly allow them to compensate for imperfect test signals, which in turn makes it more difficult to isolate the instrument characteristics. In effect, such instruments act as "golden" receivers, raising the recurring question: is it the source or is it the receiver?

The imperfect response of a coherent receiver in the complex plane may result from a number of physical impairments, such as polarization misalignment and finite extinction, output path skew, limited detector bandwidth and gain imbalance, or quadrature angle error. Methods exist to measure some of these impairments; two lasers (described later) can be used to measure the quadrature angle [6], [12] and the output path skew [12]. However, a generalized test signal that traverses beyond the unit circle would allow a broader array of receiver properties to be characterized.

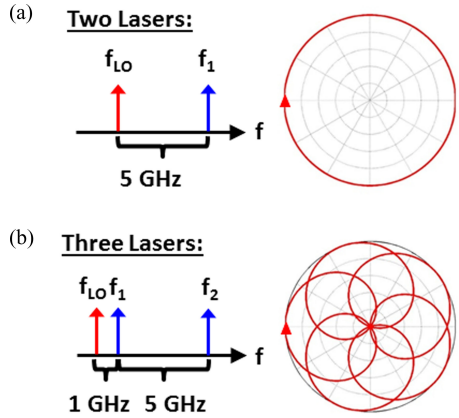

Fig. 1. The creation of heterodyne modulation patterns is illustrated for (a) two and (b) three narrowband lasers. In each case, one laser is dedicated as the local oscillator.

In this study, we describe signals for characterizing coherent optical receivers as found in both optical networks and in metrology tools for complex modulation analysis. We generate a family of complex modulation patterns based on a combination of narrow frequency tones that can be accurately predicted from first principles. We chose to demonstrate the utility of these patterns by characterizing the digital bandwidth and detector gain imbalance of a receiver, and anticipate that they can be effectively applied to many other receiver properties. The work presented here improves upon and greatly expands our preliminary demonstration of this technique [13].

II. Heterodyne Calibration Signals

Our characterization approach is based on a high-accuracy heterodyne technique used for the calibration of high-speed photoreceivers to frequencies greater than 50 GHz [4]. As demonstrated here, our technique is a simplistic form of optical arbitrary waveform generation by use of a few sinusoidal tones. The characterization of radio-frequency equipment often uses a similar multi-tone approach because these signals are easy to control and can be accurately known [14]. Fig. 1 illustrates the simple cases of complex pattern generation by use of two and three single-frequency tones or monochromatic lasers. A single laser (red) serves as the local oscillator and the remaining lasers (blue) act as the signal applied to a coherent optical receiver. In the two-laser example shown in Fig. 1(a), the demodulated signal in the complex plane traces out a trajectory restricted to the unit circle, such that the phase varies continuously but the amplitude remains constant. The pattern completes one rotation at a rate determined by the difference frequency between the two lasers, which in this example is 5 GHz. This simple pattern is useful for characterizing some receiver properties, such as the quadrature angle [12]. Fig. 1(b) illustrates the more complicated scenario involving a signal composed of two lasers, resulting in a demodulated pattern that sweeps through the interior of the unit circle five times. In both cases, the in-phase and quadrature components vary continuously, but only the three-laser case has continuous variation of both amplitude and phase. As shown, the three-laser case traces one complete pattern at a rate of 1 GHz, and the number of lobes in the pattern is determined by the ratio of the laser difference frequencies. By simply adjusting the difference frequencies, the pattern coverage within the complex plane can be altered. It can be shown that the three-laser case can also be used to characterize the quadrature angle of a coherent receiver.

Considering in more detail the case of three lasers (one local oscillator (LO) and two signal (S) lasers), we can describe the electric field of the signal E_s and the local oscillator E_{LO} as

$$E_s(t) = E_1 e^{i(\omega_1 t+\theta_1)} + E_2 e^{i(\omega_2 t+\theta_2)} \tag{1}$$

$$E_{\mathrm{LO}}(t) = E_{\mathrm{LO}} e^{i(\omega_{\mathrm{LO}} t+\theta_{\mathrm{LO}})} \tag{2}$$

where the subscripts 1, 2, and LO denote the three lasers, each having amplitudes E, frequency ω, and phase θ. Demodulating E_s in a quadrature optical receiver with E_{LO} as the local oscillator, followed by square-law balanced detection, gives the in-phase (I) and quadrature (Q) voltage signals proportionally as

$$I(t) \propto E_s(t)\cdot E_{\mathrm{LO}}(t)^* + E_s(t)^*\cdot E_{\mathrm{LO}}(t) \tag{3}$$

$$Q(t) \propto E_s(t)\cdot E_{\mathrm{LO}}(t)^* e^{-i\pi/2} + E_s(t)^*\cdot E_{\mathrm{LO}}(t) e^{i\pi/2}. \tag{4}$$

More specifically, in terms of the electric-field components of each laser, we have

$$\begin{aligned} I(t) \propto{}& E_1\cdot\cos((\omega_1-\omega_{\mathrm{LO}})t+\theta_1-\theta_{\mathrm{LO}}) \\ &+ E_2\cdot\cos((\omega_2-\omega_{\mathrm{LO}})t+\theta_2-\theta_{\mathrm{LO}}) \end{aligned} \tag{5}$$

$$\begin{aligned} Q(t) \propto{}& E_1\cdot\sin((\omega_1-\omega_{\mathrm{LO}})t+\theta_1-\theta_{\mathrm{LO}}) \\ &+ E_2\cdot\sin((\omega_2-\omega_{\mathrm{LO}})t+\theta_2-\theta_{\mathrm{LO}}). \end{aligned} \tag{6}$$

The shape of the modulation pattern in the complex plane described by $I(t)$ and $Q(t)$ is determined by the amplitude of E_1 relative to E_2, and the frequency differences between ω_1, ω_2, and ω_{LO}. If the three lasers are phase-locked to each other, the phase offsets θ_1, θ_2, and θ_{LO} are all constant with time and their values will determine only the angular orientation of the modulation pattern, but not the shape. The pattern plotted in Fig. 1(b) was obtained by plotting (5) and (6) in the complex plane with $E_1 = E_2$ at a difference frequency of $(\omega_1-\omega_2)/2\pi = 5$ GHz. The LO laser was offset by 1 GHz from one of the signal lasers, as shown in the figure, and the phase terms θ_1, θ_2, and θ_{LO} were all set to zero.

III. Experimental Setup

Fig. 2 shows the experimental setup for generating calibration test signals with three lasers near 1550.0 nm and the optical connections to a coherent optical receiver used to visualize the generated patterns. Two 10 mW fiber lasers with linewidth specifications of less than 1 kHz and 1 nm or 125 GHz of wavelength tuning were combined to form the measurement signal. The optical phase-locked-loop system [4], [15] that controlled their difference frequency applied feedback to an internal piezoelectric tuning element in one of the laser cavities as well as an external acousto-optic modulator for fast phase corrections. The third laser, which served as an LO for the optical receiver, was

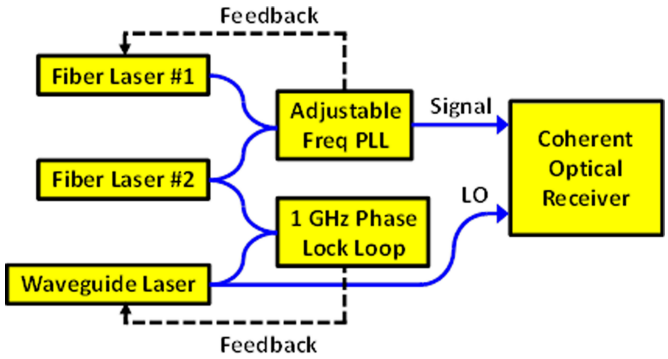

Fig. 2. The experimental system used to generate known complex modulation patterns and characterize coherent optical receivers. PLL: phase-locked loop; LO: local oscillator.

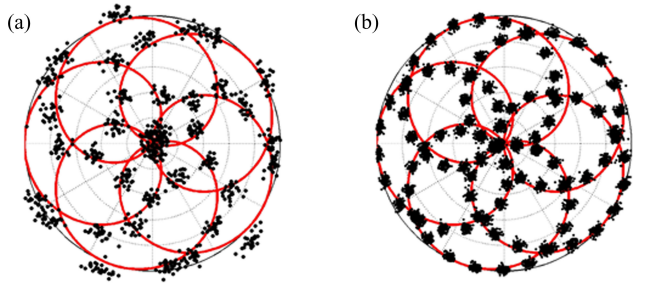

Fig. 3. The generation of a 5 GHz modulation pattern (a) before and (b) after software demodulation and signal processing. The solid red curve is the theoretical prediction; in (b) the measured signal is represented with 20 samples/symbol, where a symbol is one lobe.

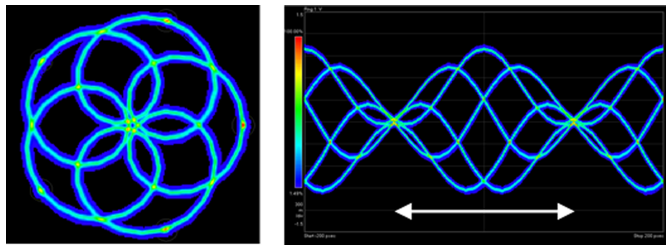

Fig. 4. Persistence plots of the complex plane (left) and eye diagram (right) for the measurement of the 5 GHz modulation pattern shown in Fig. 3. The EVM at the tips of the lobes is 2.8%; the white arrow in the eye diagram indicates the duration of one symbol or lobe.

a semiconductor waveguide laser with a linewidth specification of 5 kHz. Feedback to this laser from a second phase-locked loop was applied through direct modulation of the laser current. Both of the optical phase-lock systems used a double-heterodyne technique to control the optical difference frequencies between the lasers by use of sinusoidal RF synthesizers [4]. Adjusting the synthesizer frequencies changed the difference frequencies between the lasers, which resulted in various patterns generated in the complex plane. In all the measurements presented here, the difference frequency between fiber laser #2 and the LO laser was fixed at exactly 1 GHz, whereas the frequency between fiber lasers #1 and #2 was varied. In a further experimental simplification, the power from the two fiber lasers was made equal to within 1% for all measurements. The combined signal power was 650 μW, whereas the LO laser had an optical power of about 8 mW.

The coherent optical receiver we characterized was embedded in a commercial optical modulation analyzer (OMA), and utilized polarization-diversity quadrature optical hybrids with 40 GHz balanced detection. The electrical measurement of the detected signals was provided by a free-running, four-channel, real-time oscilloscope with a 13 GHz bandwidth sampling at 40 GSa/s. The 13 GHz bandwidth of the OMA limited the maximum pattern frequency that we could measure and present in this study. However, in principle, the pattern frequencies are only limited by the tuning range of the lasers and the ability to electrically mix them with an RF synthesizer for phase locking. At difference frequencies above 40 GHz, harmonic mixers may be used that would extend the patterns to 125 GHz and beyond. We characterized the receiver within an OMA for experimental simplicity, yet our technique is equally applicable to stand-alone receivers when supported by appropriate instrumentation. In the remainder of this paper, we refer to our coherent receiver as an OMA.

IV. Modulation Pattern Measurements

A. Pattern Demodulation

We set our lasers to the difference frequencies illustrated in Fig. 1(b) to create what we refer to as a 5 GHz modulation pattern. Fig. 3(a) shows the measurement after detection, quadrature computation, and signal normalization, as black dots in the complex plane. For comparison, the continuous red curve illustrates the theoretical prediction from Fig. 1(b) based on (5) and (6). The clustering of the dots indicates time synchronization between the real-time sampling and the generation rate of the pattern. The position of the clusters loosely conforms to the predicted curve. After applying a five-state amplitude phase-shift keying (APSK) software demodulation with constellation points uniformly spaced on the unit circle, the agreement between the measurement and prediction becomes very good, as shown in Fig. 3(b). The specified constellation points correspond to the tips of the five lobes of the modulation pattern. The software processing performs time synchronization, phase tracking, and re-sampling for a display of 20 samples per symbol, where a symbol is one lobe of the modulation pattern.

Fig. 4 shows persistence plots of this same experimental result, using smooth interpolation and digital filtering to present a measured modulation pattern that is very well defined. The error vector magnitude (EVM) calculated locally about the constellation points at the tips of the signal lobes is only 2.8% from an exponential root-mean-square average with $\alpha = 0.1$ [16]. This EVM is a little higher than the 1.6% noise floor typically observed for this instrument using two lasers [see Fig. 1(a)] and no noise insertion. An uncertainty analysis of these complex signals and their measurement is beyond the scope of this paper. Also shown in the same figure is the measured eye-diagram for one quadrature of the signal, with the distance indicated between the two null points corresponding to the temporal duration of one lobe.

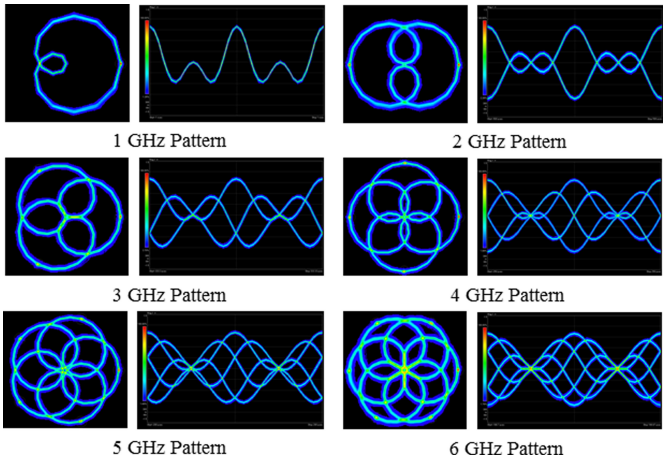

Fig. 5. Experimentally generated three-laser modulation patterns for signal difference frequencies between 1 and 6 GHz. In each case, the APSK demodulation was configured with the number of states on the unit circle equal to the number of lobes in the pattern.

B. Modulation Pattern Complexity

The complexity of the modulation patterns could easily be varied by changing the laser difference frequencies. We varied the frequency between the signal lasers by 1 GHz increments while the offset frequency to the LO was kept constant at 1 GHz. Fig. 5 presents a collection of patterns with signal difference frequencies between 1 GHz and 6 GHz that were generated experimentally with our three-laser system. In each case, the APSK demodulation was specified by making the number of constellation points equal to the number of outer lobes. The clean modulation patterns were shown to have excellent agreement with predicted curves. In this particular experimental implementation, we operated at difference frequencies up to 10 GHz, limited by the bandwidth of the RF mixer used for phase locking. Using a higher bandwidth mixer would have easily allowed us to operate at many tens of gigahertz, with abundant optical power to maintain good signal-to-noise ratio. Our fiber lasers had nearly identical center frequencies, so the highest difference frequency we could generate would be about 125 GHz, limited by the 1 nm tuning range. Higher frequencies could be generated with lasers having more tuning range or offset center frequencies.

Just as easily, a much higher level of pattern complexity was achieved when the ratio of the difference frequencies between the lasers was not an integer. Fig. 6 illustrates the case where the frequency between the signal lasers was 6.25 GHz while the LO was still offset by 1 GHz. The modulation pattern exhibits 25 lobes in the complex plane, where four is the lowest integer multiplier that makes the frequency ratio an integer. It should be emphasized that Fig. 6 is an experimental result and not a theoretical prediction, in which the OMA was able to demodulate and resolve all of the trajectories in the complex plane despite the high level of complexity.

The electrical bandwidth required to measure a pattern is dictated by the maximum difference frequency present, which as illustrated in Fig. 1(b) is between f_{LO} and f_2, and is 1 GHz higher than the pattern frequency. The appearance or shape of the pattern also depends on the relative orientation of the lasers. If the difference frequency between the signal lasers is 5 GHz but the LO laser is positioned between the signal lasers and 1 GHz away, the pattern will still have five lobes but the trajectories and shape will be different.

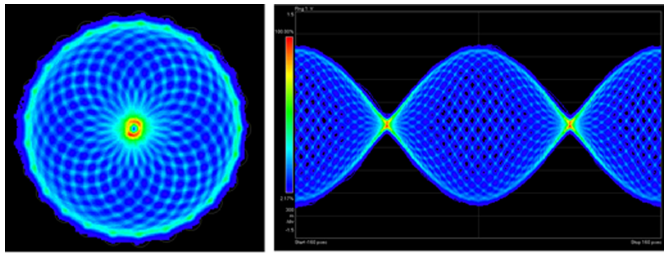

Fig. 6. A complicated modulation pattern is generated by use of non-integer frequency ratios and successfully measured. In this case, the signal difference frequency was 6.25 GHz, resulting in 25 lobes.

C. Modulation Pattern Stability and Accuracy

Signals intended for instrument calibration should in general possess a high level of stability and accuracy. The more deterministic a modulation pattern is, the more it will characterize the OMA hardware rather than the software. However, examining an unstable signal can indicate the degree to which the signal-processing capabilities of an OMA are utilized to obtain a meaningful measurement result.

We took great care to produce heterodyne-based modulation patterns with high temporal stability and accuracy for the purposes of this unambiguous demonstration, primarily by using optical phase-locked loops and narrow-bandwidth lasers. The modulation patterns were reproducible and stable in phase over the 5 μs duration of each real-time measurement. This observation is consistent with the fact that the kilohertz laser linewidths should result in temporal stabilities of more than 100 μs even without a phase lock, assuming that the difference frequencies can be set appropriately. As we will discuss, it may be possible to relax some of these hardware requirements. Referring back to Fig. 2, it should be also noted that the signal and LO are delivered to the OMA on separate optical paths of a couple of meters each. Slow thermal drift between the signal and LO did occur, but was not found to be significant over our measurement durations.

To examine the fast phase stability, we measured the 5 GHz modulation pattern with the phase-locked loop turned off. Fig. 7(a) shows the raw measurement before demodulation, which closely resembles the scattering of the phase-locked measurement points of Fig. 3(a). Fig. 7(b) shows the unlocked pattern after five-state APSK demodulation, which strongly resembles the signal quality of Fig. 3(b). The EVM calculated at the tips of the lobes is 3.6%, which is slightly noisier than the 2.8% EVM for the data of Fig. 3 that were later evaluated in Fig. 4. Therefore, over our 5 μs measurement duration the stability added by the phase-locked loop was fairly insignificant. In this scenario, a useful calibration test signal could have been constructed without the complication and expense of phase-locking optics and electronics. However, when conducting longer

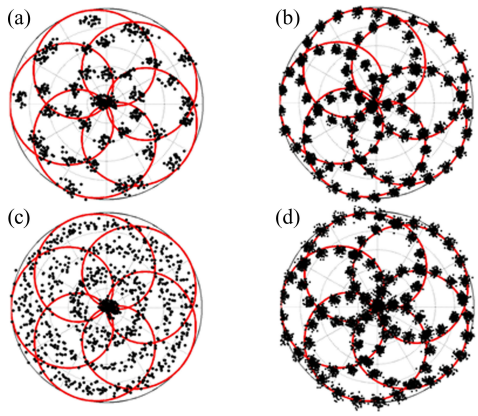

Fig. 7. The pattern stability and accuracy is demonstrated. In (a) the phase-locked loop is turned off, but demodulation recovers the pattern in (b). In (c), the signal frequency is offset by 10 MHz, but demodulation still recovers the signal in (d) with more noise than in (b).

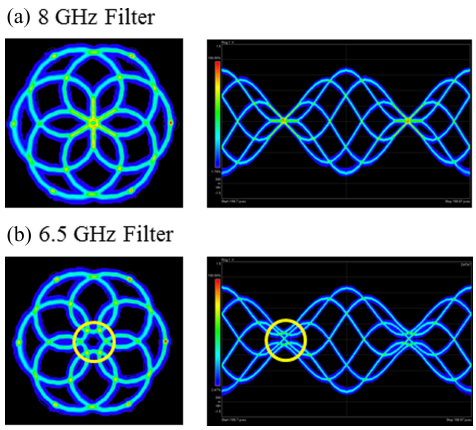

Fig. 8. The influence of modulation analyzer digital filter bandwidth is visualized. Signal distortion within the yellow circles of (b) is not apparent in (a).

measurements to achieve greater signal averaging, the stability of a phase lock may become very important.

Finally, to examine the importance of frequency accuracy, a pattern measurement was conducted with the phase-locked loop turned off, and a 10 MHz offset added to the difference frequency between the signal lasers. Fig. 7(c) shows the raw measurement with a scattering of sampling points lying in concentric rings, indicating a lack of synchronization between the sampling and the pattern generation. However, after applying five-state APSK demodulation, assuming a signal frequency of 5.00 GHz rather than the actual 5.01 GHz, the modulation pattern was resolved, as shown in Fig. 7(d). The signal processing was effective in removing the 10 MHz rotation of the modulation pattern in the complex plane. However, this result comes at the expense of slightly higher noise, with an EVM of 4.6%, as compared to the 3.6% result without the 10 MHz frequency offset [see Fig. 7(b)].

The results of Fig. 7 suggest that for some calibration scenarios, including relative comparisons or those with short durations, the requirements on the laser linewidths and phase lock performance can be relaxed. In doing so, the cost and complexity of the system can be reduced. For example, a simple wavelength lock of lasers having 1 MHz linewidths may be sufficient for a calibration measurement that lasts less than 1 μs. It should also be noted that to maintain the signal quality while relaxing the laser linewidth specification will entail a corresponding increase in the phase lock loop performance, and vice versa.

V. Coherent Receiver Characterization Examples

The value of having known modulation patterns is in their ability to quantitatively characterize the operation of measurement instruments. By adding known amounts of distortion or noise to a calibration signal, the instrument response can be isolated and quantified. Alternatively, various instrument settings can be adjusted and their impact can be quantified while measuring a known signal. While it can be easily shown that the quadrature angle of a coherent receiver can be obtained as the average phase difference between its outputs using either two- or three-laser modulation patterns [6], [12], we elected to focus on the impact of digital filtering bandwidth and detector gain imbalance of an OMA in this study.

A. Digital Filter Bandwidth

Displaying a measurement with a bandwidth that far exceeds that of the signal may add unnecessary noise. By contrast, if the bandwidth of the filtering is set too low, the measurement result may be artificially distorted. One way to detect the onset of filter distortion of an unknown but reproducible signal is to slowly decrease the bandwidth until distortion becomes observable through relative comparison. Alternatively, measurement of a known signal under a particular filtering scenario allows the distortion to be directly quantified by absolute comparison.

Fig. 8(a) presents a 6 GHz modulation pattern measured with the OMA set to a digital filter bandwidth of 8 GHz. The result can be shown to have excellent agreement with a theoretical prediction. However, the result of reducing the bandwidth to 6.5 GHz is shown in Fig. 8(b), whereby distortion in the complex plane is observed as an opening of the modulation pattern about the origin. Correspondingly, the eye diagram shows a broadening of the null point, as indicated by the yellow circle. The distortion is to be expected if the optical signal is considered more carefully. While the frequency difference between the signal lasers was only 6 GHz, the frequency differences between the two signal lasers and the LO were 1 GHz and 7 GHz. The 7 GHz frequency obviously exceeds the 6.5 GHz filter setting.

For calibration signals which have been measured as temporal waveforms, such as those obtained from a real-time OMA, it is possible to make a detailed point-by-point comparison in time to a theoretical prediction of the signal. This quantitative evaluation is accomplished by subtracting at each point in time the complex value of the measured waveform from the predicted waveform. The resulting error vector waveform can be plotted and visualized in the complex plane. While EVM is the shortest distance to the nearest constellation point and a statistical characterization [17], the error vector waveform provides information about the signal trajectories between the constellation points or bit centers, allowing the temporal location of signal

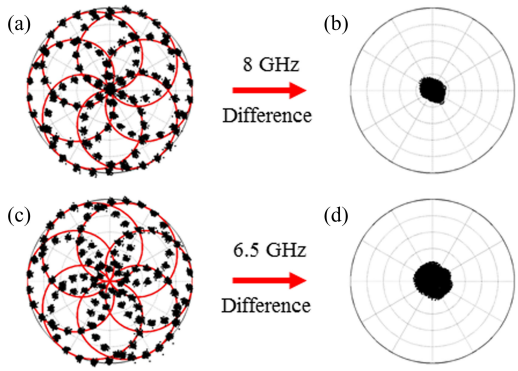

Fig. 9. The error vector waveforms (b) and (d) are the differences between the measurements (dots) and predictions (solid red curves) of (a) and (c). The measurements are from Fig. 8 and displayed with 20 samples/symbol. Each of the four plots shows the extent of the unit circle in the complex plane.

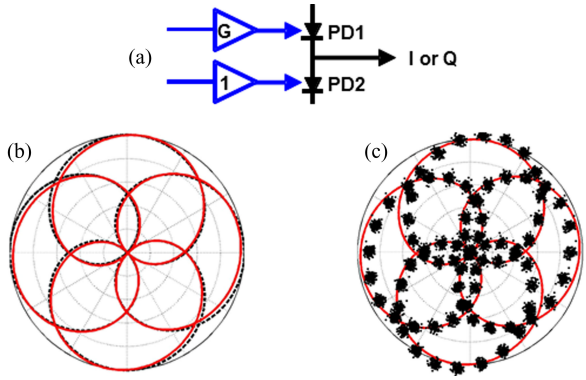

Fig. 10. Gain imbalance is modeled as illustrated in (a), where the solid red curve of (b) is $G = 0.9$ relative to $G = 1$ for the dashed black curve. Measurement of a $G \sim 0.9$ receiver is presented in (c) as dots and compared to prediction as the solid red curve.

deviations. The error vector waveform can be applied any time a measured waveform deviates from a known waveform, regardless of the cause.

Fig. 9(a) shows the 6 GHz pattern of Fig. 8(a) plotted with discrete points at 20 samples per symbol and the theoretical prediction as the red line. Fig. 9(b) plots the point-by-point difference between the measurement and prediction in the complex plane. The root-mean-square average magnitude of the error-vector waveform of Fig. 9(b) was calculated to be 8.2%, which represents the average error at all points in the complex plane covered by the known modulation. The error vector waveform is, therefore, determined at points in the complex plane for which the demodulation and signal processing may not have been optimized. For comparison, the EVM provided by the OMA at the tips of the six lobes was only 3.3% using six-state APSK demodulation. One way to improve the magnitude of an error vector waveform might be to demodulate with an APSK constellation map that defines additional points within the interior of the unit circle [18].

Fig. 9(c) and (d) shows the modulation pattern and error vector waveform, respectively, for the 6 GHz pattern with a digital filter setting of only 6.5 GHz. The filtering distortion can be seen by the larger area covered by the error-vector waveform, as compared to Fig. 9(b). The root-mean-square magnitude of the error-vector waveform was 13.2%, which is larger than the result for the 8 GHz setting. By contrast, the EVM of the distorted pattern calculated from 6-state APSK demodulation at the tips of the lobes was only 3.1%, which is lower than the 3.3% EVM of the 8 GHz setting. A lower EVM at the points specified by the constellation map is expected because the additional digital filtering removed more of the high-frequency noise. However, this also demonstrates that EVM calculated from only the limited number of constellation points can be insensitive to distortion effects.

B. Detector Gain Imbalance

Coherent optical receivers often utilize balanced detection to remove electrical contributions from unmodulated light and direct detection components. The ability to remove these unwanted contributions is described by the common-mode rejection ratio, which can depend in part on the relative signal gains of the two balanced photodiodes [19]. The gain can be viewed as the cumulative effect of insertion loss in the fiber pigtails of the detector, the coupling from the pigtails to the photodiodes, and the responsivity or electrical gain of the generated photocurrent. We considered the simplified case where only the in-phase or I balanced detector of a coherent receiver had a gain imbalance. If we model one diode of the balanced detector with unity gain and assign a relative gain G to the other diode, as illustrated in Fig. 10(a), it can be shown that the in-phase signal is

$$I_G(t) = |E_s(t)|^2 (1 - G) + \frac{I(t)}{2}(1 + G) \tag{7}$$

where $I(t)$ was defined previously by (5), and $E_s(t)$ was defined by (1). As expected, if G is close to unity, the first term in (7) becomes small, while the second term approaches $I(t)$ and the imbalance disappears. However, in the general case when G does not approach unity, it is informative to consider the relation

$$|E_s(t)|^2 = \frac{I^2(t) + Q^2(t)}{8\,|E_{\mathrm{LO}}(t)|^2} \tag{8}$$

where $|E_{\mathrm{LO}}(t)|^2$ did not vary with time in our measurement scenarios. Substituting (8) into (7) provides an expression relating the in-phase signal components with and without gain imbalance as

$$I_G(t) = \frac{I(t)}{2}(1 + G) + \frac{\left(I^2(t) + Q^2(t)\right)}{8\,|E_{\mathrm{LO}}(t)|^2}(1 - G)\,. \tag{9}$$

The first term in (9) simply scales $I(t)$ by the imbalance G. However, the numerator of the second term includes a coupling between the in-phase and quadrature components such that they are no longer strictly orthogonal. Also, the strength of this coupling is regulated by the local oscillator power through $|E_{\mathrm{LO}}(t)|^2$, where a smaller power relative to the signal power will increase the distortion. By contrast, for perfectly balanced detection, the local oscillator power only influences the signal-to-noise ratio. Fig. 10(b) plots the prediction of (9) for a 4 GHz modulation pattern with $G = 0.9$ for one quadrature. The distortion appears about an off-axis line of symmetry running from

the second to the fourth quadrant, oriented by a phase difference between the signal and local oscillator. Interestingly, along the line of symmetry, the distortion is uneven with respect to the origin.

To demonstrate detector gain imbalance, we added bend loss to one of the fiber pigtails attached to the balanced receiver inside our OMA. By using a fixed mandrel, we were able to reproduce a bend loss of approximately 10%. Fig. 10(c) shows a measured 4 GHz modulation pattern plotted over the predicted pattern, in which the type of distortion expected from Fig. 10(b) is apparent. The measured distortion is more severe than predicted and would appear to correspond to a bend loss of more than 10%. However, the optical power of the LO incident on the balanced detector relative to the signal power was not known and had to be estimated in (9). Developing a detailed measurement method in which the local oscillator power is known and kept small relative to the signal power would allow the gain imbalance to be better quantified. An error vector waveform was not created for this measurement because of uncertainty in the prediction. Regardless, it is clear that challenging measurement effects such as distortion from detector gain imbalance can be visualized with known complex modulation patterns.

VI. Discussion and Conclusion

We anticipate that the family of complex modulation patterns we have demonstrated could be applied effectively to modulation analyzers that rely on a variety of measurement techniques. Because the signals are repetitive in nature, they should be readily applicable to equivalent-time sampling and spectrum analysis methods [3], [5]–[7]. However, spectral methods may put additional restrictions on the laser difference frequencies at which meaningful results can be obtained [3]. Linear optical sampling relies on optical gating with a short-pulse local oscillator, and phase-locking this type of laser would require additional consideration. In the case of phase-sensitive nonlinear sampling, a CW local oscillator in addition to a short-pulse local oscillator is utilized. A phase lock to the pulsed local oscillator would not be required, and in fact would be extremely challenging to implement, considering the tens of nanometers it is typically located away from the signal in order to separate the nonlinear mixing products.

We have demonstrated a family of calibration signals in the complex measurement plane that are easy to control, stable, and predictable from first principles. The modulation patterns were used to test various aspects of a coherent receiver in a real-time optical modulation analyzer. The use of error-vector waveform as a performance metric enabled the quantitative evaluation of measured signal quality spanning the complex plane.

Acknowledgment

The authors gratefully acknowledge useful discussions with Dr. B. Szafraniec of Agilent Technologies and Nate Newbury of NIST.

References

[1] P. J. Winzer and R.-J. Essiambre, "Advanced modulation formats for high-capacity optical transport networks," *J. Lightw. Technol.*, vol. 24, no. 12, pp. 4711–4728, Dec. 2006.

[2] R.-J. Essiambre, G. Kramer, P. J. Winzer, G. J. Foschini, and B Goebel, "Capacity limits of optical fiber networks," *J. Lightw. Technol.*, vol. 28, no. 4, pp. 662–701, Feb. 2010.

[3] P. A. Andrekson, "Metrology of complex optical modulation formats," presented at the Optical Fiber Communications Conf. Exhib., Los Angeles, CA, USA, paper OWN1, 2011.

[4] T. Dennis and P. D. Hale, "High-accuracy photoreceiver frequency response measurements at 1.55 μm by use of a heterodyne phase-locked loop," *Opt. Exp.*, vol. 19, pp. 20103–20114, 2011.

[5] C. Dorrer, C. R. Doerr, I. Kang, R. Ryf, J. Leuthold, and P. J. Winzer, "Measurement of eye diagrams and constellation diagrams of optical sources using linear optics and waveguide technology," *J. Lightw. Technol.*, vol. 23, no. 1, pp. 178–186, Jan. 2005.

[6] P. A. Williams, T. Dennis, I. Coddington, W. C. Swann, and N. R. Newbury, "Vector signal characterization of high-speed optical components by use of linear optical sampling with milliradian resolution," *IEEE Photon. Technol. Lett.*, vol. 20, no. 23, pp. 2007–2009, Dec. 2008.

[7] M. Westlund, M. Skold, and P. A. Andrekson, "All-optical phase-sensitive waveform sampling at 40 GSymbol/s," presented at the Optical Fiber Communications Conf. Exhib., San Diego, CA, USA, paper PDP12, 2008.

[8] T. S. Clement, P. D. Hale, D. F. Williams, J. C. M. Wang, A. Dienstfrey, and D. A. Keenan, "Calibration of sampling oscilloscopes with high-speed photodiodes," *IEEE Trans. Microw. Theory Tech.*, vol. 54, no. 8, pp. 3173–3181, Aug. 2006.

[9] A. Dienstfrey, P. D. Hale, D. A. Keenan, T. S. Clement, and D. F. Williams, "Minimum-phase calibration of sampling-oscilloscopes," *IEEE Trans. Microw. Theory Tech.*, vol. 54, no. 8, pp. 3197–3208, Aug. 2006.

[10] B. Szafraniec, B. Nebendahl, and T. Marshall, "Polarization demultiplexing in stokes space," *Opt. Exp.*, vol. 18, pp. 17928–17939, 2010.

[11] T. Marshall, B. Szafraniec, and B. Nebendahl, "Kalman filter carrier and polarization-state tracking," *Opt. Lett.*, vol. 35, pp. 2203–2205, 2010.

[12] R. A. Marsland, "Challenges in design and testing of coherent receivers," presented at the Conf. Lasers Electro-Optics, San Jose, CA, USA, paper ATuB1, 2010.

[13] T. Dennis and B. Nebendahl, "Producing known complex modulation signals for calibration of optical modulation analyzers," presented at the Optical Fiber Communications Conf. Exhib., Los Angeles, CA, USA, paper OW3 H.1, 2012.

[14] N. B. Carvalho, K. A. Remley, D. Schreurs, and K. G. Gard, "Multisine signals for wireless system test and design," *IEEE Microw. Mag.*, vol. 9, no. 3, pp. 122–138, Jun. 2008.

[15] L. D'Evelyn, L. Hollberg, and Z. B. Popovic, "A CPW phase-locked loop for diode-laser stabilization," in *Proc. IEEE MTT-S Int. Microw. Symp. Dig.*, 1994, pp. 65–68.

[16] (2012). *NIST/SEMATECH e-Handbook of Statistical Methods*. [Online]. Available: http://www.itl.nist.gov/div898/handbook/

[17] R. Schmogrow, B. Nebendahl, M. Winter, A. Josten, D. Hillerkuss, S. Koenig, J. Meyer, M. Dreschmann, M. Huebner, C. Koos, J. Becker, W. Freude, and J. Leuthold, "Error vector magnitude as a performance measure for advanced modulation formats," *IEEE Photon. Technol. Lett.*, vol. 24, no. 1, pp. 61–63, Jan. 2012.

[18] N. Kikuchi, K. Mandai, K. Sekine, and S. Sasaki, "Incoherent 32-level optical multilevel signaling technologies," *J. Lightw. Technol.*, vol. 26, no. 1, pp. 150–157, Jan. 2008.

[19] Y. Painchaud, M. Poulin, M. Morin, and M Têtu, "Performance of balanced detection in a coherent receiver," *Opt. Exp.*, vol. 17, pp. 3659–3672, 2009.

Authors' biographies not available at the time of publication.